Continuum Mech. Thermodyn. (2012) 24:181–199
DOI 10.1007/s00161-011-0230-9

ORIGINAL ARTICLE

Gianpietro Del Piero · Giampiero Pampolini

The influence of viscosity on the response of open-cell polymeric foams in uniaxial compression: experiments and theoretical model

Received: 30 March 2011 / Accepted: 11 December 2011 / Published online: 6 January 2012

Abstract In a preceding paper (Pampolini and Del Piero in J Mech Mater Struct 3:969–981, 2008), the response of blocks made of a polymeric open-cell foam subject to uniaxial compression was analyzed. The hysteretic behavior exhibited in cyclic tests was interpreted within the context of nonlinear elasticity, as an effect of strain localization due to the non-convexity of the energy. Here we study some inelastic aspects of the response, such as rate dependence, strength decay after repeated loading, and memory effects. The analysis of some key experiments led us to the conclusion that viscous effects prevail over plasticity and damage. Consequently, we propose here a visco-elastic model, obtained by adding linear visco-elastic elements to our previous chain of nonlinear elastic springs. The paper is completed by the description of a series of experiments and of numerical simulations.

Keywords Polymeric foams · Strain localization · Non-convex strain energy · Solid-solid phase transition · Rate dependence

1 Introduction

Polymeric open-cell foams exhibit a complex behavior. In uniaxial compression, the stress–strain response curve shows three clearly detectable parts: an initial ascending branch, a large plateau, and a second ascending branch. While in the ascending branches the foam deforms homogeneously, in the plateau the deformation localizes along layers orthogonal to the loading direction [17,28]. At unloading, the three regimes are less clearly detectable. In cyclic loading, the stress–strain curve exhibits a hysteresis loop, and a residual deformation is observed after complete unloading [13,24].

Many studies, mostly based on numerical simulations, have been addressed to the modeling of macroscopic response in terms of microstructure [11,13,15,18,29,31]. In them, the foam is usually represented as a

Communicated by Andreas Öchsner.

G. Del Piero
Dipartimento di Ingegneria, Università di Ferrara, Via Saragat 1, 44100 Ferrara, Italy
E-mail: dlpgpt@unife.it

G. Pampolini (✉)
Laboratoire de Mécanique et d'Acoustique, 31 chemin Joseph Aiguier, 13402 Marseille, France
E-mail: pampolini@lma.cnrs-mrs.fr

Present address:
G. Pampolini
Saint-Gobain Recherche, 39, quai Lucien-Lefranc, 93303 Aubervilliers, France

periodic structure made of linear elastic beams, and strain localization is attributed to the buckling of such beams. In particular, in [13] a good agreement with the experimental loading curve was obtained by considering a periodic structure of shear-deformable linear elastic beams, whose basic element is a 14-sided polyhedron, called the Kelvin cell. A non-periodic model was proposed in [26]. In general, a numerical simulation of microscale deformation is a challenging task, because of some difficulties met in modeling the regime corresponding to the second ascending branch, see [2].

An alternative approach is to describe both strain localization and hysteresis in the context of nonlinear elasticity. This can be done by assuming a "double-well" strain energy density, which determines the presence of two phases of the material [10]. Strain localization is attributed to the phase transition, which is also the cause of the hysteresis loops observed in cyclic loading.

A purely elastic model based on this approach was proposed in [12] and developed in [24]. Here we refine this model, taking into account some inelastic aspects of the experimental response, such as

– *Stress softening*, that is, a progressive stress reduction in the subsequent cycles of a cyclic test, see Fig. 2 and the experiments in [30],
– *Memory effects*, such as the partial stress recovery observed after a sufficiently long period of rest, see Fig. 3 and the experiments in [30],
– *Rate dependence*, revealed by an increase in stress with increasing loading rate, see Fig. 7 and the experiments in [27].

While these aspects have been studied in the context of filler-reinforced rubbers and polymers, we are not aware of any specific study for foams, except the study of rate dependence made in [20]. The stress softening of filled rubbers was investigated by Mullins [22]. After him, this phenomenon was called the *Mullins effect*, though various alternative micromechanical mechanisms were proposed afterwards to interpret the same phenomenon.

In particular, in [5] the stress softening was attributed to the breaking of bonds between the polymeric chains and the filler. The breaking of the bonds was subsequently interpreted by several authors as a form of damage [3,6,8,23]. A model based on the representation of rubber as a network of polymeric chains bridged by a number of junctions variable with loading was proposed in [9], see also [7].

More recently, the presence of stress recovery induced some authors to assume a partial reconstitution of the broken bonds. For example, in the context of the theory of self-organizing linkage patterns, in [4] stress softening was attributed to a process of re-distribution of continuously destroyed and re-combined physical linkages.

A model more in line with classical continuum mechanics was obtained by interpreting the inelastic phenomena mentioned above as viscous phenomena [14,19,21]. For example, in its one-dimensional version, the model proposed in [21] consists of three rheological elements disposed in parallel: an elastic spring, a dashpot, and an elastic-plastic element, each put in series with a damage element. In [14], damage and plasticity are neglected, and the dashpot is replaced by a fractional damping element.

After performing a series of cyclic compression tests at different speeds and with different rest times between cycles, we came to the conclusion that the inelastic effects are mostly of a viscous nature. Thus, as a first approximation, we decided to neglect the effects of damage and plasticity, and to rely on a purely visco-elastic model. In this way, we came to a model that looks like an adaptation to foam rubbers of the model proposed in [14] for filled rubbers, the adaptation consisting in the replacement of the linear elastic spring by a "double-well" nonlinear elastic element. However, we did not follow [14] in taking fractional damping elements. For reasons discussed in Sect. 4.2, we preferred to take as our basic visco-elastic element a set of Maxwell elements arranged in parallel, corresponding to a Boltzmann-Volterra linear visco-elastic relaxation function made of a sum of exponentials.

The resulting rheological model has the shape of a chain, each element of which consists of a nonlinear elastic spring connected in parallel with a linear visco-elastic element. A further visco-elastic element was put in parallel with the whole chain, with the purpose of controlling the slope of the central plateau of the response curve.

In the following Sect. 2, the experiments made to identify the inelastic aspects of the response are described. Section 3 contains the description of the theoretical model, and Sect. 4 deals with the identification of the material constants. The short Sect. 5 provides some essential information on the numerical procedure, Sect. 6 is devoted to a comparison between experiments and numerical simulations, and the final Sect. 7 deals with the conclusions.

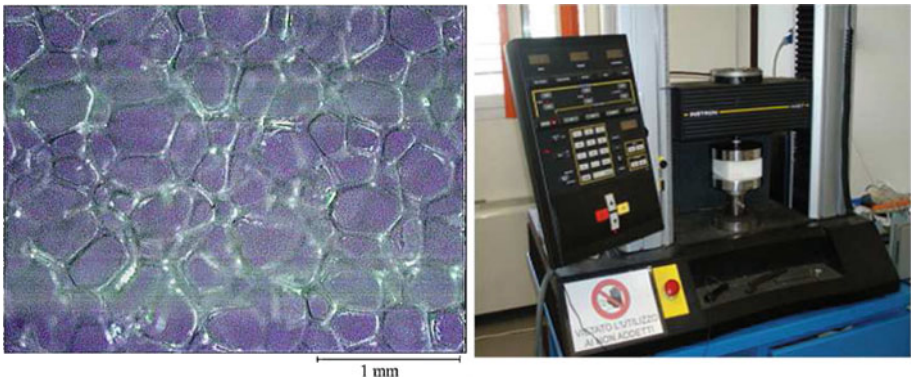

Fig. 1 The cellular structure of the polyurethane foams (*left*) and the test equipment (*right*)

2 Experiments

Our experimental analysis was addressed to the study of the inelastic effects mentioned in the Introduction. Rather than to an exhaustive characterization of the material, the experiments were addressed to getting some essential information on the rate-dependent aspects of the response in the case of uniaxial compression.

All tests were made using a load frame Instron 4467 with a 500 N load cell, located at the Laboratorio di Materiali Polimerici of the University of Ferrara. The specimens had the shape of parallelepipeds, with base dimensions 100 × 100 mm, cut out from a 50 mm thick sheet of a commercial polyether urethane foam manufactured by Chemical Resine SAS (Lissone, Italy). The mass density of the foam is 270 N/m^3, and its cellular structure is shown in Fig. 1a.

The cutting was done manually, using a ribbon saw. A pre-load of 2–3 N was applied to guarantee a full initial contact between plate and specimen. The testing equipment is shown in Fig. 1b. All tests were made at room temperature. Though the room was air-conditioned, small temperature changes in long-duration experiments are not excluded.

The load was applied by controlling the displacement of the upper crosshead, and measuring the force exerted by the sample. In what follows, *stress* denotes the force divided by the initial area, and *deformation* denotes the ratio between the upper crosshead displacement and the initial distance of the upper crosshead from the fixed lower basis. Compressive deformations and forces are taken to be positive.

2.1 Cyclic compression tests

Cyclic compression tests were performed on three samples, at a crosshead speed of 5 mm/min. At loading, the direction of motion of the upper crosshead was reversed when the deformation reached the value 0.7. At unloading, it was reversed when the load cell measured a zero force. The test was stopped after four cycles.

The stress–deformation curves are shown in Fig. 2. For the loading curves, there is a significant stress decay between the first and second cycle, and a less significant reduction afterwards. There is also a change in shape in the subsequent cycles, with a more gradual transition from the first ascending branch to the plateau, and a shortening of the plateau's length. The unloading curves are almost the same for all cycles, and there is a slight increase in the residual deformation at the end of each cycle. The overall behavior of cyclic response agrees with the experiments in [13]. There is also some similarity with the softening behavior of filled rubbers, known as the Mullins effect [22].

2.2 Four-cycle cyclic tests

To detect the presence of stress recovery, a sample was subjected to four series of cyclic tests, separated by three resting periods of increasing duration: 16 h, 52 h, 33 days. Each series consisted of four cycles. During the resting periods, the sample was kept stress-free and unconstrained.

The force–elongation curves are shown in Fig. 3. One sees that the loading curve of the first cycle in the second test, Fig. 3b, almost coincides with the loading curve of the second cycle in the first test, Fig. 3a.

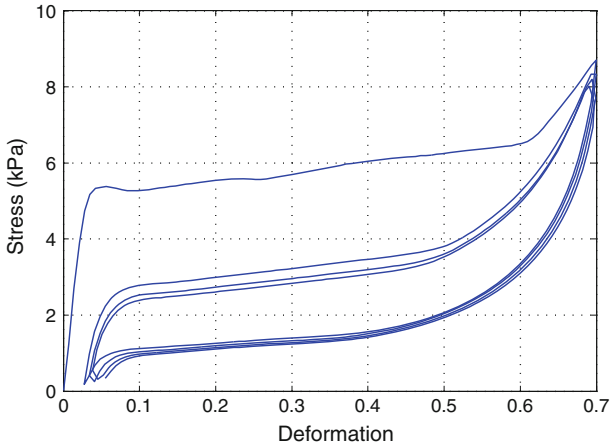

Fig. 2 Cyclic compression test with a crosshead speed of 5 mm/min. Force–elongation curves (average on three samples)

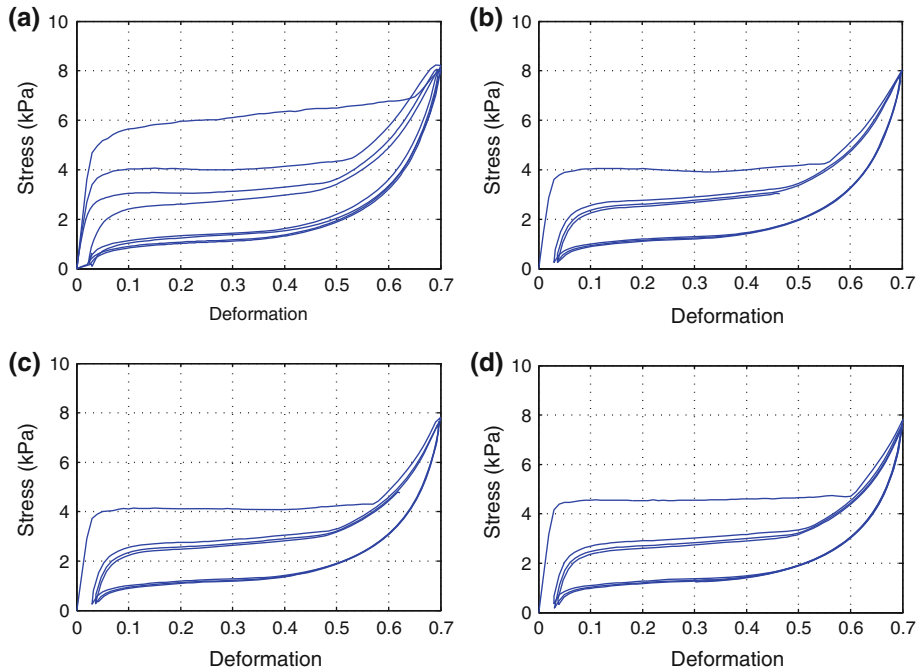

Fig. 3 Four-cycle cyclic test. Stress–deformation curves for a virgin sample (**a**), and for the same sample after three resting periods of 16 h (**b**), 52 h (**c**) and 33 days (**d**) (a single sample, crosshead speed of 5 mm/min)

Thus, after a resting period of 16 h the stress reduction observed in the last two cycles of the initial test has been recovered. In the third test performed after a further rest of 52 h there is no significant change in the response curve. On the contrary, in the fourth test, after a rest period of 33 days, the loading curve of the first cycle steps up of about 10%, from 4 kPa to almost 4.5 kPa. This evidence of stress recovery in time led us to exclude that the stress softening observed in a cyclic test be entirely due to permanent damage.

2.3 Small-amplitude cyclic tests

Small-amplitude cyclic tests were performed to detect the inelastic effects not related with phase changes. The force–elongation curve in Fig. 4a shows the hysteresis loops exhibited in loading–unloading cycles starting from the upper plateau. In the test shown in Fig. 4b, the loading–unloading cycle was interrupted several times, each time keeping the specimen under constant elongation for a duration of 45 min. The stress relaxation observed during both loading and unloading makes evident the presence of viscous effects.

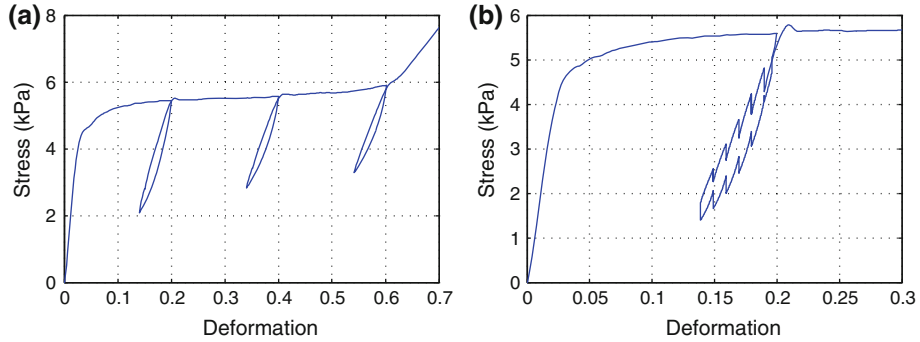

Fig. 4 Force–elongation curves for loading–unloading tests inside the hysteresis loop starting from the upper plateau, at constant speed (**a**), and with intermediate rests of 45 min (**b**) (a single sample, crosshead speed of 1 mm/ min)

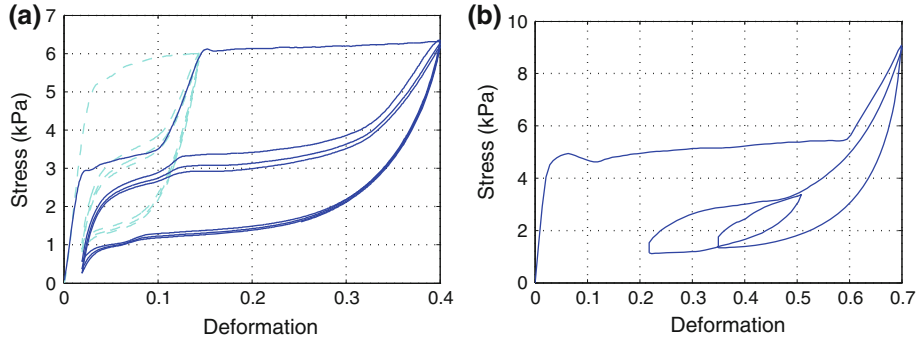

Fig. 5 a Force–elongation curves for a test made of two series of four cycles each, with two different amplitudes. **b** Force–elongation curves for a test made of three cycles of different amplitudes (a single sample, crosshead speed of 5 mm/ min)

2.4 Complex loading–unloading tests

To see the influence of the past deformation history on the shape of the loading–unloading curves, a specimen was subjected to four loading–unloading cycles with a maximum deformation of 0.15, followed by four cycles with a maximum deformation of 0.40. The curves in Fig. 5a shows that the response in the second series of cycles is different from that of a virgin specimen. Indeed, there are bumps, both in the loading and, less evident, in the unloading curves. The bumps, located in the range of the deformations applied in the first series of cycles, show that the material keeps memory of the past deformation history.

The results of a cyclic test made of cycles of variable amplitude are shown in Fig. 5b. In it, the deformation alternates between the maxima and minima

$$0,\ \ 0.70,\ \ 0.35,\ \ 0.50,\ \ 0.22,\ \ 0.70.$$

It is interesting that, at the end of this complex loading program, the specimen almost exactly goes back to the loading curve recorded in the first cycle.

2.5 Relaxation tests

Two series of tests were performed to determine the properties of stress relaxation. Theoretically, the relaxation function is defined by an ideal test, in which a deformation is applied instantaneously and then kept constant. In practice, the time required to apply the deformation is small but finite. The duration of the loading process depends on the crosshead speed allowed by the loading machine. In our case, the maximum speed allowed by the machine was 250 mm per minute.

With this speed, three specimen were loaded up to the deformation of 0.70 and then kept at this deformation for 72 h. The measured decay of the stress in time is shown in Fig. 6a, which refers to the average in the three specimen. The relaxation is very fast in the first few minutes, and much slower afterwards. A very similar response has been observed in high-damping rubbers [1].

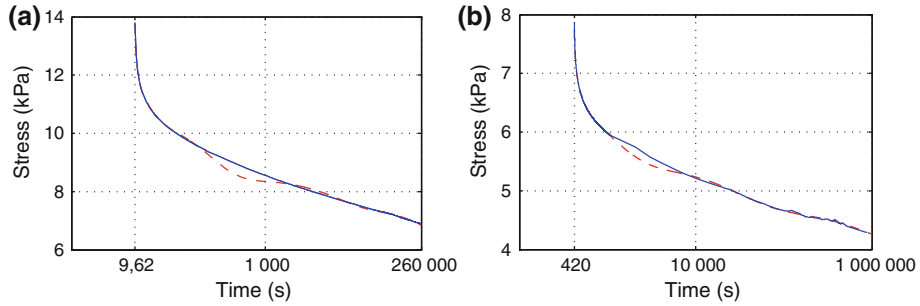

Fig. 6 Relaxation tests at a deformation of 0.7, reached with crosshead speeds 250 mm/ min (**a**) and 5 mm/min (**b**). Comparison between the experimental curves (*full lines*) and the curves (*dashed lines*) obtained from a relaxation function with the material parameters given in Tables 2 and 3, respectively

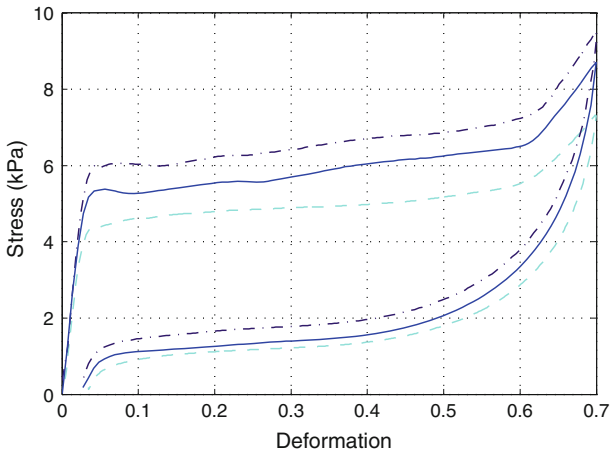

Fig. 7 Compression tests at different rates. Force–elongation curves at the crosshead speeds 0.1 mm/min (*dashed line*), 5 mm/ min (*solid line*), and 100 mm/min (*dashed-dotted line*). Average on three samples

To see the dependence of the response on the initial crosshead speed, a test was made with initial speed of 5 mm/ min. The test was made on a single sample, for a duration of 10 days. The result is shown in Fig. 6b. A comparison of the two response curves will be made later.

2.6 Tests at different velocities

The effects of the loading rate were tested by performing compressive loading–unloading cycles at the constant velocities of 0.1, 5, and 100 mm/ min. Three samples were tested for each velocity. The average stress–deformation curves in Fig. 7 show that an increase of the loading rate determines an overall rising of the loading curves. The same effect is present, but less important, in the unloading curves. The residual deformation is almost independent of the loading velocity. These tests make evident the rate-dependent character of the response.

3 The mechanical model

3.1 The basic rheological elements

The proposed model is a combination of two basic rheological elements, elastic, and dissipative. The elastic element is a nonlinear elastic spring. In a time-dependent elongation process $t \mapsto \varepsilon(t)$, the force in the spring at the time t is

$$\sigma^e(t) = w'(\varepsilon(t)), \tag{1}$$

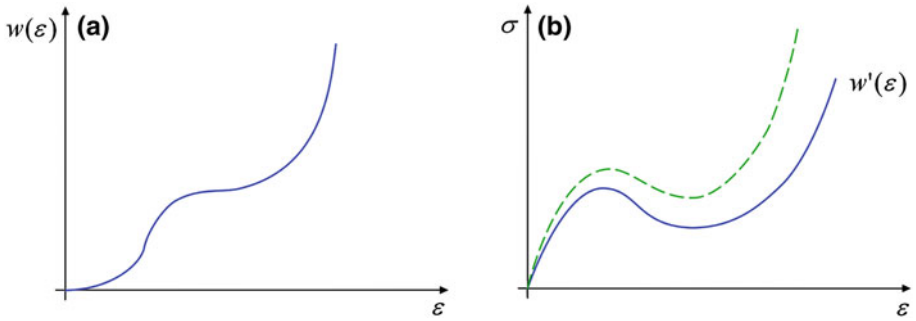

Fig. 8 The shape of the energy of a single element (**a**) and of its derivative (**b**). The *dashed line* in (**b**) shows the response of the element to a loading process with a constant strain rate

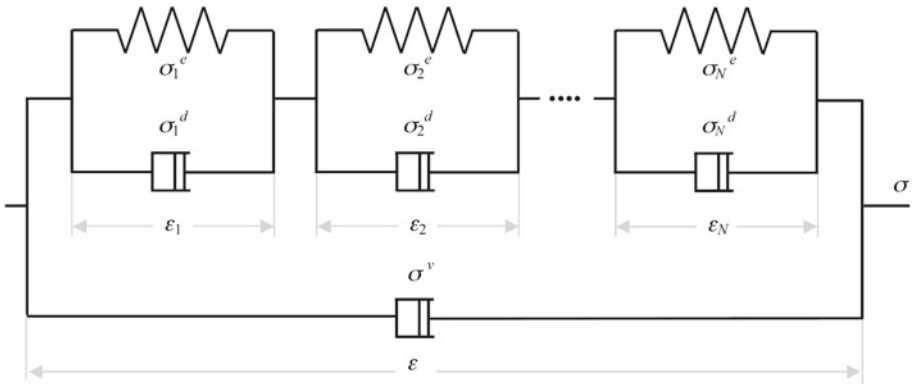

Fig. 9 The basic rheological model. Notice that springs and dashpots are graphical representations of the constitutive law (1) and (2), respectively

where w is the energy of the spring, and the apex denotes differentiation with respect to ε. For w, the non-convex shape shown in Fig. 8a is assumed. While the force in the spring only depends on the current value $\varepsilon(t)$ of the elongation, the force in the dissipative element, which is assumed to obey the linear viscoelastic Boltzmann-Volterra law

$$\sigma^d(t) = G(0)\,\varepsilon(t) + \int_0^\infty \dot{G}(s)\,\varepsilon(t-s)\,\mathrm{d}s, \tag{2}$$

depends both on the current value and on the past history of ε. The *relaxation function* G is assumed to be $C^2(0,\infty)$, with $G(s)$ positive and $\dot{G}(s)$ negative for all s. Its analytic expression will be discussed later.

3.2 The model

The proposed model is shown in Fig. 9. It consists of a chain of N elements, set in parallel with a single dissipative element. Each element in the chain is composed of two subelements, one elastic and one dissipative, set in parallel. They are represented in a conventional way by a spring and a dashpot, though their constitutive laws are in fact the laws (1) and (2), respectively.

Denote by $\varepsilon_i(t)$ the elongation of the i-th element, and by $\varepsilon(t)$ the total elongation of the chain

$$\varepsilon(t) = \sum_{i=1}^{N} \varepsilon_i(t). \tag{3}$$

The force acting on an element is the sum of the forces in the two subelements

$$\sigma^c(t) = w'(\varepsilon_i(t)) + G(0)\,\varepsilon_i(t) + \int_0^\infty \dot{G}(s)\,\varepsilon_i(t-s)\,\mathrm{d}s, \qquad i \in \{1, \dots N\}. \tag{4}$$

The force is the same for all elements, while the elongations $\varepsilon_i(t)$ and the partial forces $\sigma_i^e(t)$ and $\sigma_i^d(t)$ may be different for different elements. For the single dissipative element out of the chain, the elongation is again $\varepsilon(t)$, and the force is

$$\sigma^v(t) = \Gamma(0)\,\varepsilon(t) + \int_0^\infty \dot{\Gamma}(s)\,\varepsilon(t-s)\,\mathrm{d}s, \tag{5}$$

with a relaxation function Γ different, in general, from G. The total force acting on the chain is

$$\sigma(t) = \sigma^c(t) + \sigma^v(t). \tag{6}$$

3.3 The evolution problem

We assume that at all times $t < 0$ the chain is at rest, with $\varepsilon_i(t) = 0$ for all i. For $t \geq 0$, we prescribe an elongation process $t \mapsto \varepsilon(t)$, with initial condition $\varepsilon(0) = 0$. With these data, the total force is

$$\sigma(t) = w'(\varepsilon_i(t)) + G(0)\,\varepsilon_i(t) + \int_0^t \dot{G}(s)\,\varepsilon_i(t-s)\,\mathrm{d}s + \Gamma(0)\,\varepsilon(t) + \int_0^t \dot{\Gamma}(s)\,\varepsilon(t-s)\,\mathrm{d}s. \tag{7}$$

We wish to solve the following evolution problem:

Problem $\mathcal{P}1$. *Given the process $t \mapsto \varepsilon(t)$, find processes $t \mapsto \sigma(t)$, $t \mapsto \varepsilon_i(t)$ such*

(i) $\varepsilon_i(0) = 0$ *for all i,*
(ii) $\sum_i \varepsilon_i(t) = \varepsilon(t)$ *for all $t > 0$,*
(iii) *Equation (7) holds for all $t > 0$ and for all i.*

3.4 The infinitesimal incremental problem

Approximate solutions to problem $\mathcal{P}1$ can be constructed via time discretization, using an incremental approach. By differentiation of (7), one has[1]

$$\dot{\sigma}(t) = \big(w''(\varepsilon_i(t)) + G(0)\big)\,\dot{\varepsilon}_i(t) + \int_0^t \dot{G}(s)\,\dot{\varepsilon}_i(t-s)\,\mathrm{d}s, + \Gamma(0)\,\dot{\varepsilon}(t) + \int_0^t \dot{\Gamma}(s)\,\dot{\varepsilon}(t-s)\,\mathrm{d}s, \tag{8}$$

and, with the positions

$$\begin{aligned} Q_i &\doteq w''(\varepsilon_i(t)) + G(0), \\ A_i &\doteq \int_0^t \dot{G}(s)\,\dot{\varepsilon}_i(t-s)\,\mathrm{d}s + \Gamma(0)\,\dot{\varepsilon}(t) + \int_0^t \dot{\Gamma}(s)\,\dot{\varepsilon}(t-s)\,\mathrm{d}s, \end{aligned} \tag{9}$$

[1] Here and in the following, a superimposed dot denotes the *right* derivative with respect to t. Our regularity assumptions guarantee the existence of $\dot{\sigma}$, $\dot{\varepsilon}$, $\dot{\varepsilon}_i$, and $\dot{G}$ at all t.

one gets the N equations

$$\dot{\sigma} = Q_i \dot{\varepsilon}_i + A_i, \tag{10}$$

one for each i. The coefficients Q_i and A_i are known: Q_i is a function of the current elongation $\varepsilon_i(t)$, and A_i depends on the past history of ε_i at the time t. Together with the equality

$$\sum_{i=1}^{N} \dot{\varepsilon}_i = \dot{\varepsilon}, \tag{11}$$

obtained by the differentiation of (3), these equations determine the following incremental problem:

Problem $\mathcal{P}2$. *Given Q_i, A_i and the right derivative $\dot{\varepsilon}$ of the total elongation at t, find the right derivatives $\dot{\varepsilon}_i$, $\dot{\sigma}$ at t which solve the system (10), (11).*

Equations (10) and (11) form a system of $N + 1$ linear algebraic equations, whose coefficients form the matrix

$$H = \begin{Bmatrix} Q_1 & 0 & 0 & \dots & -1 \\ 0 & Q_2 & 0 & \dots & -1 \\ 0 & 0 & Q_3 & \dots & -1 \\ \dots & \dots & \dots & \dots & \dots \\ 1 & 1 & 1 & \dots & 0 \end{Bmatrix}, \tag{12}$$

with determinant

$$\det H = \sum_{i=1}^{N} \left(\prod_{j \neq i} Q_j \right). \tag{13}$$

The system has a unique solution if $\det H \neq 0$. There may be no solutions when $\det H = 0$. This occurs, for example, when $Q_1 = Q_2 = 0$ and $A_1 \neq A_2$. Moreover, the system is ill-conditioned when $\det H$ is close to zero. To deal with such singular cases, we re-formulate the problem in terms of finite increments, evaluated over a small, but finite, time interval τ.

3.5 The finite incremental problem

For each i, writing Eq. (7) at the instants t and $t + \tau$ and subtracting yields

$$\begin{aligned} \delta\sigma = {} & w'(\varepsilon_i(t) + \delta\varepsilon_i) - w'(\varepsilon_i(t)) + G(0)\,\delta\varepsilon_i + \Gamma(0)\,\delta\varepsilon \\ & + \int_0^{t+\tau} \dot{G}(s)\,\varepsilon_i(t+\tau-s)\,\mathrm{d}s - \int_0^{t} \dot{G}(s)\,\varepsilon_i(t-s)\,\mathrm{d}s \\ & + \int_0^{t+\tau} \dot{\Gamma}(s)\,\varepsilon(t+\tau-s)\,\mathrm{d}s - \int_0^{t} \dot{\Gamma}(s)\,\varepsilon(t-s)\,\mathrm{d}s, \end{aligned} \tag{14}$$

with $\delta\sigma = \sigma(t+\tau) - \sigma(t)$, $\delta\varepsilon = \varepsilon(t+\tau) - \varepsilon(t)$, and $\delta\varepsilon_i = \varepsilon_i(t+\tau) - \varepsilon_i(t)$. After splitting the first integral into two parts and after some changes of variable, the difference of the first two integrals takes the form

$$\int_0^{\tau} \dot{G}(s)\,\varepsilon_i(t+\tau-s)\,\mathrm{d}s + \int_0^{t} (\dot{G}(s+\tau) - \dot{G}(s))\,\varepsilon_i(t-s)\,\mathrm{d}s,$$

and integrating by parts one gets

$$\begin{aligned} & \int_0^{\tau} G(s)\,\dot{\varepsilon}_i(t+\tau-s)\,\mathrm{d}s + G(\tau)\varepsilon_i(t) - G(0)\varepsilon_i(t+\tau) \\ & \quad + \int_0^{t} (G(s+\tau) - G(s))\,\dot{\varepsilon}_i(t-s)\,\mathrm{d}s - (G(\tau) - G(0))\,\varepsilon_i(t). \end{aligned}$$

By approximating, in the time interval $(t,\ t+\tau)$, the derivative $\dot{\varepsilon}_i$ with the constant $\delta\varepsilon_i/\tau$, we get the final form

$$\bar{G}_\tau\,\delta\varepsilon_i - G(0)\,\delta\varepsilon_i + \int_0^t (G(s+\tau) - G(s))\,\dot{\varepsilon}_i(t-s)\,\mathrm{d}s,$$

with

$$\bar{G}_\tau = \frac{1}{\tau}\int_0^\tau G(s)\,\mathrm{d}s.$$

A similar transformation can be done on the last two integrals in (14). After this, the expression of $\delta\sigma$ becomes

$$\begin{aligned}\delta\sigma \;=\; & w'(\varepsilon_i(t)+\delta\varepsilon_i) - w'(\varepsilon_i(t)) + \;\bar{G}_\tau\,\delta\varepsilon_i \\ & + \int_0^t (G(s+\tau) - G(s))\,\dot{\varepsilon}_i(t-s)\,\mathrm{d}s + \;\bar{\Gamma}_\tau\,\delta\varepsilon + \int_0^t (\Gamma(s+\tau) - \Gamma(s))\,\dot{\varepsilon}(t-s)\,\mathrm{d}s,\end{aligned}$$

and after setting

$$\begin{aligned} f_\tau(\varepsilon) \;&\doteq\; w'(\varepsilon) + \bar{G}_\tau\varepsilon, \\ B_i \;&\doteq\; \int_0^t (G(s+\tau) - G(s))\,\dot{\varepsilon}_i(t-s)\,\mathrm{d}s + \bar{\Gamma}_\tau\,\delta\varepsilon + \int_0^t (\Gamma(s+\tau) - \Gamma(s))\,\dot{\varepsilon}(t-s)\,\mathrm{d}s,\end{aligned}$$

the equations

$$\delta\sigma \;=\; f_\tau(\varepsilon_i + \delta\varepsilon_i) - f_\tau(\varepsilon_i) + B_i. \tag{15}$$

follow. Together with the discretized version of (3),

$$\delta\varepsilon \;=\; \sum_{i=1}^N \delta\varepsilon_i, \tag{16}$$

they form a system of $N+1$ nonlinear algebraic equations in the unknowns $\delta\varepsilon_i$, $\delta\sigma$. Thus, the finite incremental version of problem $\mathcal{P}2$ is as follows:

Problem $\mathcal{P}3$. *Given* $\tau>0$, ε_i, B_i, *and* $\delta\varepsilon$, *find the increments* $\delta\varepsilon_i$, $\delta\sigma$ *which solve the system* (15), (16).

The Eqs. (10), (11) of the linear incremental problem are re-obtained in the limit when $\tau\to 0$.

3.6 The first phase transition

Consider a process $t\mapsto\varepsilon(t)$ with $\dot{\varepsilon}(t)>0$ for all $t\geq 0$. Because at $t=0$, the coefficients $A_i=\Gamma(0)\,\dot{\varepsilon}(0)$ and $Q_i = w''(0)+G(0)$ are the same for all i and all Q_i are positive, there is a time interval $(0,t_A)$ in which the infinitesimal problem $\mathcal{P}2$ has the homogeneous solution

$$\dot{\varepsilon}_i = \frac{1}{N}\,\dot{\varepsilon}, \qquad \dot{\sigma} = \frac{1}{N}\,Q_i\,\dot{\varepsilon} + A_i,$$

with the same Q_i and the same A_i for all i. This homogeneous regime ends at the instant t_A at which all Q_i simultaneously reach the value zero. At this instant, the determinant (13) becomes equal to zero, and the system (10), (11) reduces to

$$\dot{\sigma} = A_i, \qquad \sum_{i=1}^N \dot{\varepsilon}_i = \dot{\varepsilon}.$$

There is an infinity of solutions to this problem, since only the sum of the $\dot{\varepsilon}_i$ is determined. In particular, the homogeneous solution $\dot{\varepsilon}_i = N^{-1}\dot{\varepsilon}$ is highly unstable because, as we see below, a small perturbation of the data A_i and Q_i is sufficient to determine a completely different evolution of the system for $t \geq t_A$.

More stable solutions are obtained by assuming a certain dispersion of the data, which renders the Q_i slightly different from each other. In this case, there is a spring, say $i = 1$, which attains the value $Q_i = 0$ before the others. At the instant t_A at which this occurs, one has

$$Q_1 = 0, \qquad Q_i > 0 \quad \forall i > 1,$$

and the system (10), (11) has the unique solution

$$\dot{\sigma} = A_1, \qquad \dot{\varepsilon}_i = \frac{A_1 - A_i}{Q_i} \quad \forall\, i > 1, \qquad \dot{\varepsilon}_1 = \dot{\varepsilon} - \sum_{i=2}^{N} \dot{\varepsilon}_i, \tag{17}$$

in which, from (9),

$$A_1 - A_i = \int_0^{t_A} \dot{G}(s)\left(\dot{\varepsilon}_1(t_A - s) - \dot{\varepsilon}_i(t_A - s)\right) \mathrm{d}s.$$

Because the spring $i = 1$ is the first to reach the critical value $\varepsilon_i(t_A)$, we may admit that at the instants preceding t_A the derivative $\dot{\varepsilon}_1$ is slightly larger than the remaining $\dot{\varepsilon}_i$. Then, by the negativeness of $\dot{G}$,

$$A_1 - A_i < 0.$$

Then $\dot{\varepsilon}_i < 0$ for all $i > 1$ by (17), and finally, by (11),

$$\dot{\varepsilon}_1 = \dot{\varepsilon} - \sum_{i=2}^{N} \dot{\varepsilon}_i > \dot{\varepsilon}. \tag{18}$$

That is, the elongation $\dot{\varepsilon}_1$ of the first spring is larger than the given elongation $\dot{\varepsilon}$ of the chain. Therefore, a slight dispersion of the data determines a solution in which the deformation localizes at a single spring.

A localized deformation is in general too large to be properly described in terms of infinitesimal increments. A better description is obtained in terms of finite increments. Consider the finite incremental problem $\mathcal{P}3$ with the data

$$\varepsilon_i = \varepsilon_A, \quad B_i = B_A, \qquad \forall i \in \{1, \ldots N\}, \tag{19}$$

where $\varepsilon_A = \varepsilon(t_A)$, and B_A is a given constant. Such data correspond to a homogeneous deformation of the chain, in which all elements have the same past history and reach simultaneously the critical elongation ε_A. Writing equation (15) for two elements i, j, and subtracting, we get the equations

$$f_\tau(\varepsilon_A + \delta\varepsilon_i) = f_\tau(\varepsilon_A + \delta\varepsilon_j), \qquad i, j \in \{1 \ldots N\}. \tag{20}$$

These are N^2 equations, $(N - 1)$ of which independent. Together with (16), they form a $N \times N$ system of nonlinear equations in the unknowns $\delta\varepsilon_i$. The system has many solutions. Indeed, for any fixed, sufficiently small $\delta\varepsilon_i$, for each j there are three elongations $\varepsilon_A + \delta\varepsilon_j$ which satisfy equation (20), one on each of the two ascending branches and one on the descending branch of the curve f_τ.

In the infinitesimal problem, strain localization corresponds to a solution in which one elongation, say ε_1, jumps to the second ascending branch, while all remaining ε_i jump back to the same point in the first ascending branch. For the analogous solution of the finite problem, Eqs. (16) and (20) reduce to the 2×2 system

$$f_\tau^I(\varepsilon_A + \delta\varepsilon_i) = f_\tau^{II}(\varepsilon_A + \delta\varepsilon_1), \qquad \delta\varepsilon_1 + (N - 1)\,\delta\varepsilon_i = \delta\varepsilon, \tag{21}$$

where f_τ^I, f_τ^{II} are the restrictions of f_τ to the two ascending branches, and i is any index different from 1. The elongation

$$\xi \doteq \delta\varepsilon_1 - \delta\varepsilon = -(N - 1)\,\delta\varepsilon_i$$

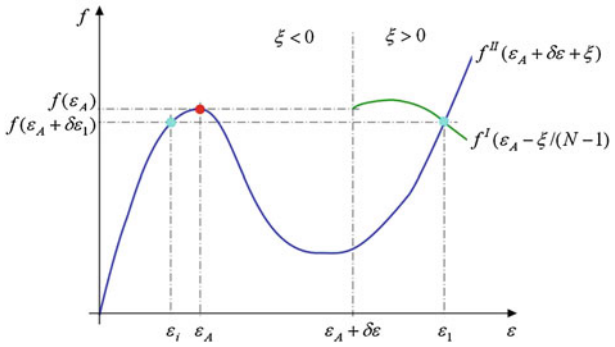

Fig. 10 The localized solution of the finite incremental problem at the first phase transition

represents the deviation from the ideal situation in which the total elongation $\delta\varepsilon$ localizes on the first spring. With this new variable, the system (21) reduces to the single equation

$$f_\tau^I(\varepsilon_A - \xi\,(N-1)^{-1}) = f_\tau^{II}(\varepsilon_A + \delta\varepsilon + \xi). \tag{22}$$

This solution corresponds to the intersection of the curves $\xi \mapsto f_\tau^I(\varepsilon_A - \xi\,(N-1)^{-1})$ and $\xi \mapsto f_\tau^{II}(\varepsilon_A + \delta\varepsilon + \xi)$, see Fig. 10.

We say that f_τ^I and f_τ^{II} characterize the *phase* A and the *phase* B of the material, respectively. Therefore, the solution of (22) describes the situation in which the spring $i = 1$ undergoes a transition from phase A to phase B, while all remaining springs remain in phase A.

With further increasing $\varepsilon(t)$, a situation is reached in which $\varepsilon_1(t)$ is in phase B and all remaining $\varepsilon_i(t)$ reach the limit value ε_A. At this point, we consider the solution in which a second spring, say $i = 2$, undergoes the phase transition. This is the solution of the 3×3 system

$$\begin{aligned} f_\tau^{II}(\varepsilon_1 + \delta\varepsilon_1) - f_\tau^{II}(\varepsilon_1) + B_1 &= f_\tau^{II}(\varepsilon_A + \delta\varepsilon_2) - f_\tau^I(\varepsilon_A) + B_2, \\ f_\tau^I(\varepsilon_A + \delta\varepsilon_i) &= f_\tau^{II}(\varepsilon_A + \delta\varepsilon_2), \\ \delta\varepsilon_1 + \delta\varepsilon_2 + (N-2)\,\delta\varepsilon_i &= \delta\varepsilon. \end{aligned}$$

The procedure is repeated, until all springs undergo the phase change.

3.7 The subsequent phase transitions

Consider a cyclic process in which $\varepsilon(t)$ oscillates between zero and some $\varepsilon_{\max}$, sufficiently large to allow the springs to undergo the phase change. During the unloading part of the first cycle the elongations ε_i decrease. When they are close to the minimum value ε_B attainable in phase B, the determinant (13) becomes small, and there is again numerical instability.

Again, this determines a localized solution, better described by the finite incremental problem. Let ε_1 be the smallest of the ε_i. Take the solution in which ε_1 jumps back to phase A, while all remaining ε_i stay in phase B. Because the ε_i and the B_i are now all different, the phase change is governed by equation (16) plus the $(N-1)$ equations

$$f_\tau^I(\varepsilon_1 + \delta\varepsilon_1) - f_\tau^{II}(\varepsilon_1) + B_1 = f_\tau^{II}(\varepsilon_i + \delta\varepsilon_i) - f_\tau^{II}(\varepsilon_i) + B_i, \qquad i \in \{2, \dots N\}.$$

For decreasing $\varepsilon(t)$, the situation is reached in which a second spring, say $i = 2$, reaches the limit value ε_B. Then this spring undergoes the phase transition, and so on, until all springs return in phase A. A similar procedure applies to all subsequent cycles.

4 The choice of the material constants

4.1 The elastic energy

In our paper [24], for the spring we took an energy density of the form

$$w(F) = \tfrac{1}{2}\,\alpha\, F \cdot F + \Upsilon(\det F),$$

Table 1 The values of the material constants for the nonlinear elastic springs

c (kPa)	m	μ (kPa)	a	β (kPa)	k
85	15	2.5	0.4	3.3	18

Table 2 The values of the material constants for the relaxation functions G and Γ, obtained by fitting the relaxation test with initial crosshead speed of 5 mm/min

	G		Γ		
j	1	2	3	4	5
K_j (kPa)	5.25	1.09	34.8	1.81	0.99
η_j (kPa s)	437	34.8×10^3	370	17.4×10^2	10.3×10^5

where F is the gradient of the three-dimensional deformation, and α is a positive constant. From it, with an appropriate choice of the function Υ, we deduced the one-dimensional stress-deformation relation

$$w(\varepsilon) = \frac{1}{2}\alpha\,(1+\varepsilon)^2 + c\,(1+\varepsilon)^m\left(\frac{1}{m+2}\,(1+\varepsilon)^2 - \frac{1}{m}\right) \\ -\mu\log(1+\varepsilon) + \frac{\beta\sqrt{\pi}}{2\sqrt{k}}\,\mathrm{erf}\left(\sqrt{k}(1+\varepsilon-a)\right) + \gamma, \tag{23}$$

where erf $(\cdot)$ is the error function

$$\mathrm{erf}(x) = \frac{2}{\sqrt{\pi}}\int_0^x \exp(-t^2)\,\mathrm{d}t, \tag{24}$$

c, m, μ, β, k, a are positive constants, and the constants

$$\alpha = \mu - \beta\exp(-k(a-1)^2), \\ \gamma = -\frac{1}{2}(\mu - \beta\exp(-k(a-1)^2)) + \frac{2c}{m(m+2)} - \frac{\beta\sqrt{\pi}}{2\sqrt{k}}\,\mathrm{erf}(\sqrt{k}\,(a-1)), \tag{25}$$

are determined by the condition that both strain energy and force be zero at the reference configuration $\varepsilon = 0$. The expression of the force

$$\sigma^e(\varepsilon) = (1+\varepsilon)\left(\mu - \beta\exp(-k\,(a-1)^2)\right) + c\,(1+\varepsilon)^{m-1}((1+\varepsilon)^2 - 1) \\ -\mu\,(1+\varepsilon)^{-1} + \beta\exp(-k(1+\varepsilon-a)^2), \tag{26}$$

is obtained by differentiation of (23).

The values assumed in the numerical simulations for the remaining constants are shown in Table 1. They differ from those given in [24]. Indeed, while the latter were chosen to fit the overall experimental loading curve under confined compression, the values in Table 1 refer to the elastic part of the deformation, to a complete loading–unloading cycle, and to unconfined compression. The identification procedure was made in two steps: first, a study of the influence of each constant on the shape of the elastic response curve; then, a series of numerical simulations on the the first cycle of the loading–unloading curves. The difference between experiments and simulations was minimized using an optimization routine based on the Hooke and Jeeves method. In the simulations, a chain of 120 elements and the visco-elastic constants of Table 2 were used. More details on the identification procedure can be found in [25].

4.2 The relaxation functions

In the model, there are two types of dissipative elements: those present in each element of the chain and the single dissipative element out of the chain. The two types of elements are supposed to account for the viscous properties of the cell walls and of the bulk foam, respectively.

Table 3 The values of the material constants for the relaxation functions G and Γ, obtained by fitting the relaxation test with initial crosshead speed of 250 mm/min

	G		Γ		
j	1	2	3	4	5
K_j (kPa)	2.60	4.27	33.9	3.56	1.23
η_j (kPa s)	366	58.7×10^5	21.6	24	16.3×10^4

In the tests shown in Fig. 6, the applied initial deformation of 0.7 was sufficiently large to exclude nonhomogeneous effects in the relaxation process. Therefore, one may suppose that the experimental curves reproduce the sum of the relaxation functions, G and Γ, of the two elements.

As shown in Fig. 6b, for the relaxation curve with the initial deformation applied at the speed of 5 mm/ min, an accurate fitting was obtained by a relaxation function made of the sum of five exponentials

$$G(t) + \Gamma(t) = \sum_{j=1}^{5} K_j \exp\left(-\left(\frac{K_j\, t}{\eta_j}\right)\right). \tag{27}$$

The relaxation test does not provide any information about the distribution of the exponentials between the external and internal elements. However, some information can be drawn from the slope of the loading curve in the plateau regime.

Indeed, there are two main sources of viscous deformation: the intrinsic viscosity, and the viscosity due to the presence of pore gas. The first is a bulk property, common to all volume elements, and is represented by the external viscous damper. The second only concerns the cell walls, and is represented by the internal elements.

The intrinsic viscosity gives a positive contribution to the plateau's slope, while the pore gas, finding some obstacle to its outflow, produces a pneumatic damping effect that opposes the collapsing of the cell walls. This surface effect has a negligible influence on the plateau's slope. Therefore, the positive slope of the plateau measured in the experiments can be used to fix the proportion between the external and internal elements.

In our case, the best approximation to the measured slope was obtained by considering two exponentials for G and three exponentials for Γ. The best values of the constants K_j and η_j, obtained with a least-square procedure, are given in Table 2. See [25] for further details.

The same operations made on the relaxation curve with initial crosshead speed of 250 mm/ min gave the result shown in Table 3. The large difference between the two sets of constants dramatically shows the inadequacy of linear visco-elasticity to describe the rate-dependent behavior of the material under study. On this point, the proposed model needs a further refinement. Nevertheless, for the purpose of the present paper, the constants in Table 2 are acceptable. Indeed, all relevant cyclic tests have been made at the same constant speed of 5 mm/ min, and we will see below that for this specific speed the response is satisfactory.

Remaining within the limits of linear visco-elasticity, it is well known that an excellent fitting with a small number of elements can be obtained using fractional elements, see e.g., [16]. We considered this possibility, but we eventually discarded it for a number of reasons. The first is that the complication of computations with fractional exponents cancels the advantage, in terms of computational time, of working with a smaller number of elements. A second reason is that the derivative of a relaxation function made of fractional elements is singular at the origin. Under this circumstance, any determination of the constant $G(0)$ becomes unreliable. This gives serious numerical problems at the phase transitions, at which the solutions of the incremental problem strongly depend on that constant.

Finally, the specific structure of the exponential function provides a decisive advantage in computing the history terms in an iterative procedure. For example, consider the term

$$C(t) = \int_0^t \exp(-ks)\, \dot{\varepsilon}(t-s)\, \mathrm{d}s, \tag{28}$$

which is a part of the history term $A_i(t)$ defined in (9). With the change of variable $r = t - s$ it transforms into

$$C(t) = \exp(-kt) \int_0^t \exp(kr)\, \dot{\varepsilon}(r)\, \mathrm{d}r. \tag{29}$$

Then at the time $t+\tau$,

$$C(t+\tau) = \exp(-k(t+\tau)) \left(\int_0^t \exp(kr)\, \dot{\varepsilon}(r)\, \mathrm{d}r + \int_t^{t+\tau} \exp(kr)\, \dot{\varepsilon}(r)\, \mathrm{d}r \right)$$
$$= \exp(-k\tau) \left(C(t) + \exp(-kt) \int_t^{t+\tau} \exp(kr)\, \dot{\varepsilon}(r)\, \mathrm{d}r \right). \tag{30}$$

With this separation of the contributions at t and τ, the term $C(t+\tau)$ need not be re-calculated at each iteration step. Moreover, approximating $\dot{\varepsilon}(r)$ with a constant in the interval $(t, t+\tau)$, one obtains the recursive formula

$$C(t+\tau) = \exp(-k\tau)\, C(t) + (1 - \exp(-k\tau))\, \frac{\dot{\varepsilon}}{k}, \tag{31}$$

which, at every step, provides $C(t+\tau)$ as an explicit function of τ.

5 Numerical simulations

In the numerical simulations, we considered the chain represented in Fig. 9, subject to strain-controlled loading processes $t \to \varepsilon(t)$. As already observed in [24], if the number N of the elements of the chain is not sufficiently large, unrealistic oscillations appear in the response curves. The number $N = 120$ came out to be large enough to avoid this undesired effect.

In all simulations, the material constants given in Tables 1 and 2 were used. The evolution problem $\mathcal{P}1$ was solved iteratively, starting from the initial state $\sigma(0) = \varepsilon_i(0) = 0$. Time discretization was made by taking time intervals of duration 0.03 s. In each interval, the strain rate $\dot{\varepsilon}(t)$ was approximated by its average over the same interval.

At the initial time of each interval, the determinant (13) was computed. If $\det H$ was greater than 10^{-2}, or if it had not changed sign, the linear algebraic system (10), (11), corresponding to the infinitesimal problem $\mathcal{P}2$, was solved. Otherwise, the finite problem $\mathcal{P}3$ was considered, and the nonlinear algebraic system (15), (16) was solved using the Newton-Raphson method.

Below, we describe the main results of our simulations, and we draw some general conclusions about the correspondence between model and experiments.

6 Comparison with experiments

In this section, we examine the correspondence of the response predicted by the model to the experimental results. For each type of test, we point out the major discrepancies and suggest some possible remedies.

6.1 Cyclic compression tests

For the cyclic compression test described in Sect. 2.1, the numerical and experimental curves are compared in Fig. 11. One sees that the model captures some main features of the experimental response, such as:

- the hysteresis loop observed in all cycles,
- the drop of the loading curve with increasing number of cycles,
- the sharp transition from the first ascending branch to the plateau in the first cycle, and a more gradual transition in the subsequent cycles,
- the substantial independence of the unloading curves on the number of cycles,
- a residual deformation at the end of each cycle, increasing with the number of cycles.

However, there are two major discrepancies between model and experiments. The first concerns the transition between the plateau and the second ascending branch of the response curve. In the model, the transition is sharp and occurs at a deformation almost independent of the number of cycles, while in the experiments, the transition is smooth and occurs at a deformation which gradually decreases, passing from almost $\varepsilon = 0.6$ at the first cycle to about $\varepsilon = 0.5$ at the subsequent cycles.

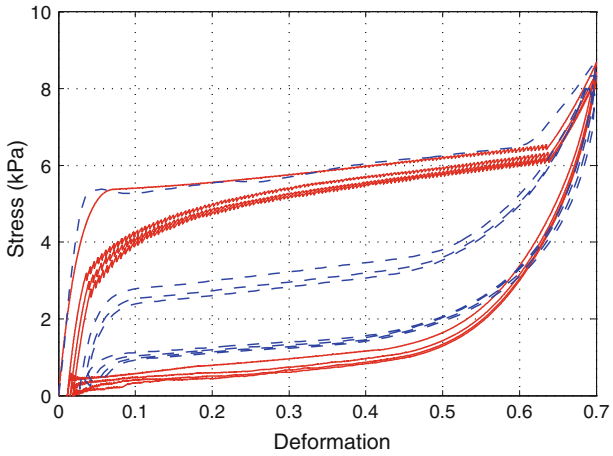

Fig. 11 Numerical simulations of a four-cycle test (*full line*) and the corresponding experiments (*dashed line*). Crosshead speed 5 mm/min

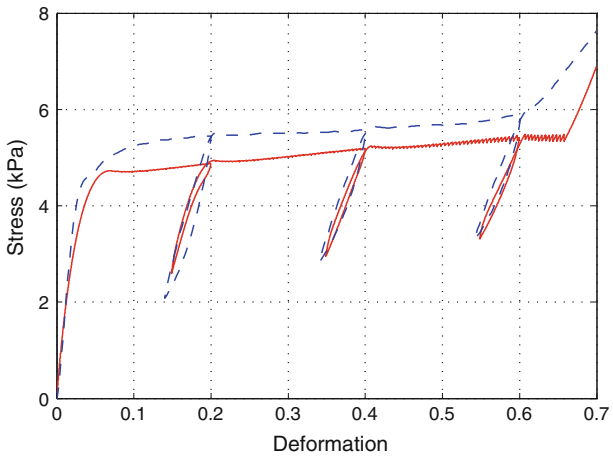

Fig. 12 Numerical (*solid lines*) and experimental (*dashed lines*) response curves for the small-amplitude cyclic tests of Fig. 4a. Crosshead speed 1 mm/min

The second discrepancy is that in the experiments, the plateaus keep approximately the same slope in all cycles, and the loading curves approach each other only after the end of the plateau regime. In the model, the loading curves approach each other more quickly, and they almost coincide for deformations larger than 0.4.

These discrepancies seem to be due to the occurring of permanent damage in the transition from the first to the second cycle. In fact, in the work in progress [25] a closer resemblance is obtained by adding some damage effects. The compatibility of permanent damage with the phenomenon of partial recovery described in Sect. 2.2 has not yet been tested.

6.2 Small-amplitude cyclic tests

A numerical simulation of the small-amplitude cyclic test described in Sect. 2.3 is shown in Fig. 12. The model correctly reproduces the observed hysteresis loops.

However, the loops are smaller than the observed ones. Indeed, the maximum drop of the stress in a loop is about 30% smaller in the simulation. This can be attributed to a nonlinear visco-elastic effect, which renders inappropriate the material constants determined for a strain rate of 5 mm/ min to reproduce the present test, which was made at the strain rate of 1 mm/ min. Similar nonlinear visco-elastic effects emerge from the subsequent experiments.

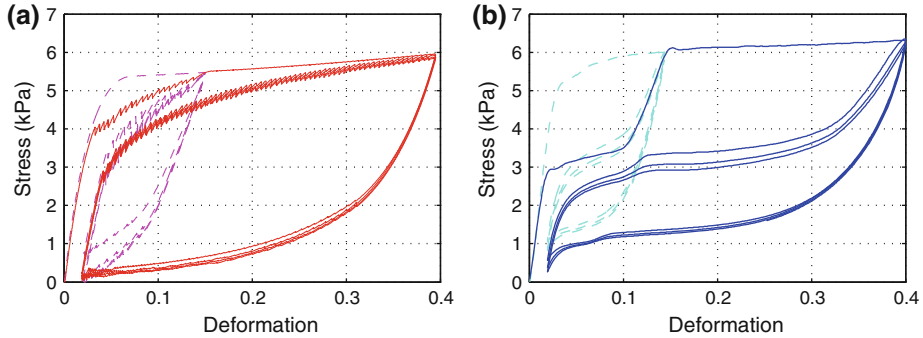

Fig. 13 Numerical (**a**) and experimental (**b**) response curves for the double cyclic test of Fig. 5a

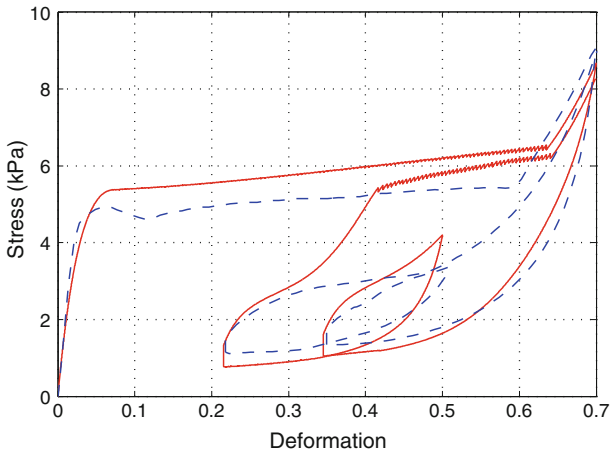

Fig. 14 Experimental (*dashed lines*) and numerical (*solid lines*) response curves for the complex cyclic test of Fig. 5b

6.3 Complex loading–unloading tests

A simulation of the double cyclic test described in Sect. 2.3 is shown in Fig. 13a. The test consists of two series of four cycles, one at small and the other one at large strain amplitudes. In the first series, a comparison with the experimental curves of Fig. 13b exhibits the same analogies and discrepancies observed in the ordinary cyclic tests. In the second series, the first loading curve stays below the same curve of the first series, but reaches it at the maximum deformation of the first series. This is in agreement with the experiment. Less satisfactory are the subsequent loading curves, in which the bump observed in the experimental curves is absent. We conjecture that the shape of the second series of curves could be improved by adding a damage term.

A simulation of the cyclic test with different amplitudes is shown in Fig. 14. Comparison with the experimental curves shows a general qualitative agreement. In particular, at the end of the process, the model reaches the first loading curve as done in the experiment. Some details are also captured, like the small vertical segments at the end of the two unloading curves, $\varepsilon = 0.35$ and $\varepsilon = 0.22$, which are due to a short rest of the machine at the moment of reversing the crosshead speed. The shape of the hysteresis cycles suffers the same defects pointed out above.

6.4 Tests at different velocities

In Fig. 15 are shown the numerical simulations of the loading–unloading tests at different velocities described in Sect. 2.6. The model correctly predicts that the stress increases with the loading rate. But there are important discrepancies with the experimental curves in Fig. 7. Indeed, as shown in Fig. 15b, the model strongly overestimates the rate dependence of the plateau's slope, while the rate dependence of the plateau's length and of the stress at the plateau's onset are underestimated.

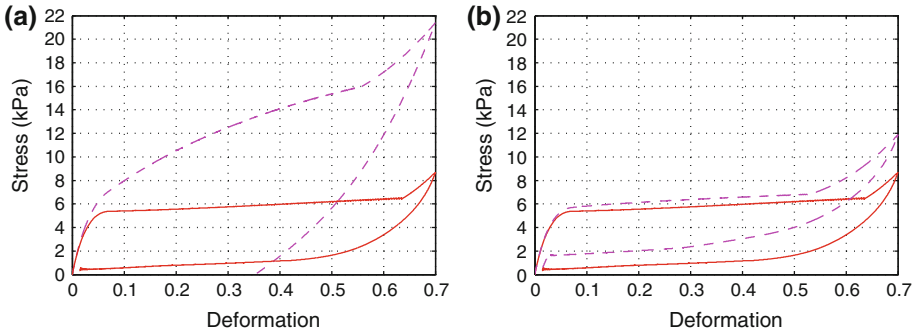

Fig. 15 Numerical simulations of loading–unloading tests at different loading rates: 5 mm/ min, and 100 mm/ min. In (**a**) the material constants in Table 2 are used for both loading rates. In (**b**), the dependence of the material constants on the loading rate is obtained by taking the values in Table 2 for the rate of 5 mm/ min, and those in Table 3 for the rate of 100 mm/min

This result reveals the strongly nonlinear character of the visco-elastic response. In fact, far better results are obtained by assuming a dependence of the visco-elastic constants on the loading rate. Indeed, the response curves shown in Fig. 15b, obtained by taking the constants in Table 2 for the speed of 5 mm/ min and the constants in Table 3 for the speed of 100 mm/ min, are much closer to the experimental curves.

7 Conclusions

Let us draw some conclusions on the efficiency of the proposed model. Generally speaking, the present visco-elastic model captures many of the observed inelastic aspects of the response, not reproduced by the previous purely elastic model [24]. However, the experiments reveal some specific aspects that, to be properly described, would require the introduction of damage. The present model shows highly nonlinear viscous effects, for which a description in terms of linear visco-elasticity is quite inadequate. More specifically, we observe that

– the visco-elastic model keeps the main feature of the purely elastic model proposed in [24], that is, the effectiveness in describing the strain localization phenomenon and the hysteresis observed in loading–unloading cycles,
– the visco-elastic model gives substantial improvements with respect to the purely elastic model in the description of complex loading processes, such as the small-amplitude loading–unloading cycles with relaxation intervals of Fig. 14,
– the comparison with experiments made in Sects. 6.2 and 6.4 picks out some specific points for which the use of a linear visco-elastic constitutive equation is insufficient,
– the comparison with experiments made in Sects. 6.1 and 6.3 show that there are some aspects of the material response which cannot be described by a purely visco-elastic model. For these aspects, the introduction of a damage variable is necessary.

The above conclusions suggest by themselves the future lines of research. For a further improvement of the model, the priorities are the adoption of nonlinear visco-elastic relations, and the introduction of damage variables. In particular, the study of the influence of damage is the object of the forthcoming paper [25].

References

1. Amin, A.F.M.S., Lion, A., Sekita, S., Okui, Y.: Nonlinear dependence of viscosity in modeling the rate-dependent response of natural and high damping rubbers in compression and shear: experimental identification and numerical verification. Int. J. Plasticity **22**, 1610–1657 (2006)
2. Bardenhagen, S.G., Brydon, A.D., Guilkey, J.E.: Insight into the physics of foam densification via numerical. Simulation. J. Mech. Phys. Solids **53**, 597–617 (2005)
3. Beatty, M.F., Krishnaswamy, S.: A theory of stress-softening in incompressible isotropic materials. J. Mech. Phys. Solids **48**, 1931–1965 (2000)
4. Besdo, D., Ihlemann, J.: Properties of rubberlike materials under large deformations explained by self-organizing linkage patterns. Int. J. Plasticity **19**, 1001–1018 (2003)
5. Bueche, F.: Mullins effect and rubber-filler interaction. J. Appl. Polymer Sci. **15**, 271–281 (1961)

6. DeSouza Neto, E.A., Perić, D., Owen, D.R.: A phenomenological three-dimensional rate-indipendent continuum damage model for highly filled polymers: formulation and computational aspects. J. Mech. Phys. Solids **42**, 1533–1550 (1994)
7. De Tommasi, D., Puglisi, G., Saccomandi, G.: A micromechanics-based model for the Mullins effect. J. Rheol. **50**, 495–512 (2006)
8. Dorfmann, A., Ogden, R.W.: A pseudo-elastic model for loading, partial unloading and reloading of particle-reinforced rubber. Int. J. Solids Struct. **40**, 2699–2714 (2003)
9. Drozdov, A.D., Dorfmann, A.: A micro-mechanical model for the response of filled elastomers at finite strains. Int. J. Plasticity **19**, 1037–1067 (2003)
10. Ericksen, J.L.: Equilibrium of bars. J. Elast. **5**, 191–201 (1975)
11. Gibson, L.J., Ashby, M.F.: Cellular Solids: Structure and Properties. 2nd edn. Cambridge University Press, Cambridge (1997)
12. Gioia, G., Wang, Y., Cuitiño, A.M.: The energetics of heterogeneous deformation in open-cell solid foams. Proc. R. Soc. Lond. A **457**, 1079–1096 (2001)
13. Gong, L., Kyriakides, S.: Compressive response of open-cell foams. Part II: initiation and evolution of crushing. Int. J. Solids Struct. **42**, 1381–1399 (2005)
14. Haupt, P., Lion, A., Backhaus, E.: On the dynamic behaviour of polymers under finite strains: constitutive modelling and identification of parameters. Int. J. Solids Struct. **37**, 3633–3646 (2000)
15. Jang, W.-Y., Kraynik, A.M., Kyriakides, S.: On the microstructure of open-cell foams and its effect on elastic properties. Int. J. Solids Struct. **45**, 1845–1875 (2008)
16. Koeller, R.C.: Applications of fractional calculus to the theory of viscoelasticity. ASME J. Appl. Mech. **51**, 299–307 (1984)
17. Lakes, R., Rosakis, P., Ruina, A.: Microbuckling instability in elastomeric cellular solids. J. Mater. Sci. **28**, 4667–4672 (1993)
18. Laroussi, M., Sab, K., Alaoui, A.: Foam mechanics: nonlinear response of an elastic 3D-periodic microstructure. Int. J. Solids Struct. **39**, 3599–3623 (2002)
19. Lion, A.: A constitutive model for carbon black filled rubber. Experimental investigations and mathematical representations. Continuum Mech. Thermodyn. **8**, 153–169 (1996)
20. Markert, B.: A biphasic continuum approach for viscoelastic high-porosity foams: comprehensive theory, numerics, and applications. Arch. Comput. Methods Eng. **15**, 371–446 (2008)
21. Miehe, C., Keck, J.: Superimposed finite elastic-viscoelastic-plastoelastic stress response with damage in filled rubbery polymers. Experiments, modelling and algorithmic implementation. J. Mech. Phys. Solids **48**, 323–365 (2000)
22. Mullins, L., Tobin, N.R.: Theoretical model for the elastic behavior of filler-reinforced vulcanized rubbers. Rubber Chem. Technol. **30**, 555–571 (1957)
23. Ogden, R.W., Roxburg, D.G.: A pseudo-elastic model for the Mullins effect in filled rubber. Proc. R. Soc. Lond. A **455**, 2861–2877 (1999)
24. Pampolini, G., Del Piero, G.: Strain localization in open-cell polyurethane foams: experiments and theoretical model. J. Mech. Mater. Struct. **3**, 969–981 (2008)
25. Pampolini, G., Raous, M.: Non linear elasticity, viscosity and damage for polymeric foams (2011, submitted)
26. Roberts, A.P., Garboczi, E.J.: Elastic properties of model random three-dimensional open-cell solids. J. Mech. Phys. Solids **50**, 33–55 (2002)
27. Sorrentino, L., Aurelia, M., Iannace, S.: A simple method to predict high strain rates mechanical behavior of low interconnected cell foams. Polym. Test. **26**, 878–885 (2000)
28. Wang, Y., Cuitiño, A.N.: Full-field measurements of heterogeneous deformation patterns on polymeric foams using digital image correlation. Int. J. Solids Struct. **39**, 3777–3796 (2002)
29. Warren, W.E., Kraynik, A.M.: Linear elastic behavior of a low-density Kelvin foam with open cells. ASME J. Appl. Mech. **64**, 787–793 (1997)
30. White, S.W., Kim, S.K., Bajaj, A.K., Davis, P.: Experimental techniques and identification of nonlinear and viscoelastic properties of flexible polyurethane foam. Nonlinear Dyn. **22**, 281–313 (2000)
31. Zhu, H.X., Mills, N.J., Knott, J.F.: Analysis of the high strain compression of open-cell foams. J. Mech. Phys. Solids **45**, 1875–1904 (1997)